Structural and Practical Identifiability of Dual-input Kinetic Modeling in Dynamic PET of Liver Inflammation

Yang Zuo[1], Souvik Sarkar[2], Michael T. Corwin[1], Kristin Olson[3], Ramsey D. Badawi[1], Guobao Wang[1,*]

1. Department of Radiology, 2. Department of Internal Medicine, 3. Department of Pathology and Laboratory Medicine, University of California at Davis

E-mail: gbwang@ucdavis.edu

Abstract. Dynamic ^{18}F-FDG PET with tracer kinetic modeling has the potential to noninvasively evaluate human liver inflammation using the FDG blood-to-tissue transport rate K_1. Accurate kinetic modeling of dynamic liver PET data and K_1 quantification requires the knowledge of dual-blood input function from the hepatic artery and portal vein. While the arterial input function can be derived from the aortic region on dynamic PET images, it is difficult to extract the portal vein input function accurately from PET. The optimization-derived dual-input kinetic modeling approach has been proposed to overcome this problem by jointly estimating the portal vein input function and FDG tracer kinetics from time activity curve fitting. In this paper, we further characterize the model properties by analyzing the structural identifiability of the model parameters using the Laplace transform and practical identifiability using Monte Carlo simulation based on fourteen patient datasets. The theoretical analysis has indicated that all the kinetic parameters of the dual-input kinetic model are structurally identifiable, though subject to local solutions. The Monte Carlo simulation results have shown that FDG K_1 can be estimated reliably in the whole-liver region of interest with reasonable bias, standard deviation, and high correlation between estimated and original values, indicating of practical identifiability of K_1. The result has also demonstrated the correlation between K_1 and histological liver inflammation scores is reliable. FDG K_1 quantification by the optimization-derived dual-input kinetic model is promising for assessing liver inflammation.

1. Introduction

Nonalcoholic steatohepatitis (NASH) is a progressive nonalcoholic fatty liver disease (NAFLD) affecting approximately 5-10 million patients in the United States [Michelotti et al., 2013, Musso et al., 2011]. The hallmark of NASH is hepatic inflammation and injury in the setting of hepatic steatosis [Wree et al., 2013]. While invasive liver biopsy is the current gold standard in clinics, dynamic ^{18}F-fluorodeoxyglucose (FDG) positron emission tomography (PET) with kinetic modeling has been demonstrated to be promising for assessing liver inflammation non-invasively by quantifying the FDG blood-to-tissue transport rate K_1 [Wang et al., 2017, Sarkar et al., 2017, Sarkar et al., 2018]. Beasue the liver recieves

dual blood supplies from the hepatic artery and portal vein, accurate liver PET kinetic modeling and quantification of K_1 require the knowledge of dual-blood input function (DBIF) [Wang et al., 2018, Munk et al., 2001]. Although the arterial input function can be derived from the aortic region on dynamic PET images, it is difficult to extract the portal vein input function from PET. The limited spatial resolution of PET and small anatomic size of the portal vein result in serious partial volume effects and high noise in the image-derived input function.

Traditional single-input kinetic modeling neglects the difference between the hepatic artery input function and portal vein input function, resulting in inaccuracy in kinetic parameter estimation [Brix et al., 2001, Munk et al., 2001]. Existing population-based DBIF approaches [Brix et al., 2001, Munk et al., 2001, Kudomi et al., 2009] use the model parameters pre-determined by population means that were commonly derived using arterial blood sampling in animal studies, which however can become ineffective in human studies. In contrast, the optimization-derived DBIF model [Wang et al., 2018] employs mathematical optimization to jointly estimate the parameters of DBIF and liver FDG kinetics. It directly utilizes image-derived arterial input function, requires no invasive arterial blood sampling, and is more adaptive to individual patients. With the improved kinetic modeling, the FDG blood-to-liver transport rate K_1 was statistically associated with histopathologic grades of liver inflammation, while K_1 by the traditional SBIF model and population-based DBIF model did not show a statistical significance [Wang et al., 2018].

Identifiability analysis is crucial for examining the stability of a kinetic model [Gunn, 1996, Mankoff et al., 2006]. It characterizes whether or not the unknown parameters of a specified model can be uniquely determined and how reliably these parameters can be estimated from noisy measurements. This concept was first brought to the field of biological system research by Bellman and Astrom [Bellman and Astrom, 1970] as an extension of studies on control systems [Kalman, 1963]. Identifiability analysis has been widely used in mathematical modeling in economy [Rothenberg, 1971], chemistry [Komorowski et al., 2011] and system biology [Raue et al., 2014] and dynamic PET [Gunn, 1996, Mankoff et al., 2006]. There are two main types of identifiabilities - structural identifiability [Bellman and Astrom, 1970, Anderson, 1983] and practical identifiability [Miao et al., 2008, Miao et al., 2011]. Structural identifiability refers to under what condition the kinetic parameters can be determined from noise-free data. Practical identifiability refers to how reliably a structurally identifiable parameter can be estimated from noisy data. Note that even if a parameter is structurally identifiable, it may not be estimated with adequate accuracy from real measurements. The analysis methods for structural identifiability include the Laplace transform [Bellman and Astrom, 1970], power series expansion [Pohjanpalo, 1978], similarity transform [Walter and Lecourtier, 1981], differential algebra [Ljung and Glad, 1994, Audoly et al., 2001, Xia and Moog, 2003] and so on [Miao et al., 2011]. The methods for practical identifiability analysis include Monte Carlo simulation [Miao et al., 2008], correlation matrix [Rodriguez-Fernandez et al., 2006a, Rodriguez-Fernandez et al., 2006b] and so on [Miao et al., 2011]. Despite its high computational cost, Monte Carlo simulation is considered as the most effective method for

analyzing the practical identifiability of a model.

In dynamic PET, most of the popular kinetic models follow the first-order ordinary differential equations with linear parameters and are commonly structurally identifiable. Hence, previous identifiability studies in dynamic PET focused on practical identifiability analysis [El Fakhri et al., 2009, Mankoff et al., 1998, Muzi et al., 2006, Doot et al., 2010, Muzi et al., 2005]. For dual-input kinetic modeling, the optimization-derived DBIF model contains two additional parameters when compared with traditional SBIF and population-based DBIF model. While the new model has improved the practical correlation of FDG K_1 with histology, it is still unclear if all the free parameters are identifiable. In addition, the increased number of free parameters may potentially increase variance in kinetic parameter estimation, but little is known so far on the quantitative aspects of the modeling.

In this paper, we conduct a theoretical analysis using the Laplace transform to assess the structural identifiability and conduct a Monte Carlo simulation to evaluate the practical identifiability using patient data of liver inflammation. The results from this study can be used to indicate the quantification accuracy and precision of model parameters and provide guidance for further improving kinetic modeling of dynamic liver PET data.

2. Structural identifiability analysis using the Laplace transform

2.1. Compartmental modeling by differential equations

Most compartmental models in dynamic PET imaging can be described by the following first-order ordinary differential equations:

$$\frac{\mathrm{d}\boldsymbol{c}(t)}{\mathrm{d}t} = \boldsymbol{A}\boldsymbol{c}(t) + \boldsymbol{b}u(t), \tag{1}$$

$$C_{\mathrm{T}}(t) = \boldsymbol{w}^T\boldsymbol{c}(t) + vu(t), \tag{2}$$

$$\boldsymbol{c}(0) = \boldsymbol{0}, \tag{3}$$

where t is time; $\boldsymbol{c}(t) = [c_1(t), c_2(t), ..., c_n(t)]^T$ is the system states which are assumed to be zero at initial time, where c_i represents the time activity of the i-th compartment and n is the number of tissue compartments; $u(t)$ is the system input, often representing the blood input function in dynamic PET; $C_{\mathrm{T}}(t)$ is the system output, i.e., the measured time activity curve (TAC) by PET; $\boldsymbol{A}$ is a n by n matrix, $\boldsymbol{b}$ is a n by 1 vector, $\boldsymbol{w}$ is a n by 1 vector and v is a scalar vector. $\boldsymbol{A}$, $\boldsymbol{b}$, $\boldsymbol{w}$ and v are composed of the kinetic parameters $\boldsymbol{\theta} = (\theta_1, \theta_2, ..., \theta_m)$ to be determined.

For a commonly used 3-compartment model (Fig. 1) such as for dynamic FDG-PET imaging, we have

$$u(t) = C_{\mathrm{p}}(t), \tag{4}$$

$$\boldsymbol{c}(t) = [C_{\mathrm{f}}(t), C_{\mathrm{m}}(t)]^T, \tag{5}$$

$$\boldsymbol{A} = \begin{bmatrix} -(k_2+k_3) & k_4 \\ k_3 & -k_4 \end{bmatrix}, \tag{6}$$

$$\boldsymbol{b} = [K_1, 0]^T, \tag{7}$$

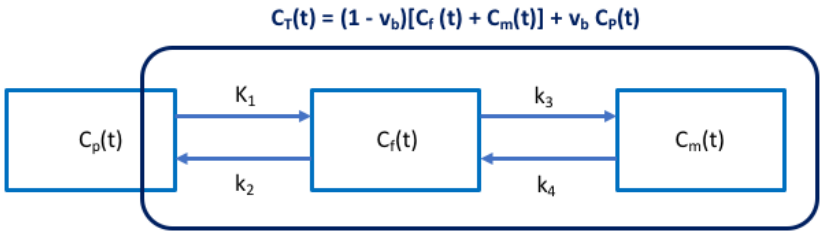

Figure 1. Three-compartment $(C_{\mathrm{p}}(t), C_{\mathrm{f}}(t), C_{\mathrm{m}}(t))$ model with single-blood input function (SBIF). $C_{\mathrm{T}}(t)$ denotes the total activity that can be measured by PET.

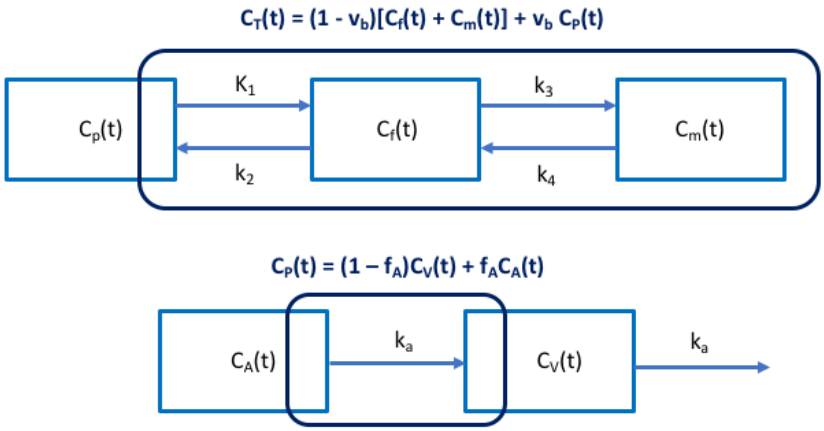

Figure 2. Optimization-derived dual-blood input function (DBIF) model. The FDG kinetic parameters $(v_b, K_1, k_2, k_3, k_4)$ and dual-input parameters (f_A, k_a) are jointly estimated by time activity curve fitting.

$$\boldsymbol{w} = [1 - v_b, 1 - v_b]^T, \tag{8}$$

$$v = v_b, \tag{9}$$

where $C_{\mathrm{p}}(t)$ is the plasma input function; $C_{\mathrm{f}}(t)$ and $C_{\mathrm{m}}(t)$ are the concentration in the free FDG and metabolized FDG compartments, respectively. The superscript "T" denotes matrix or vector transpose. $\boldsymbol{\theta} = [v_b, K_1, k_2, k_3, k_4]$ with K_1, k_2, k_3, k_4 denoting the rate constants of FDG transport among compartments. v_b denotes the fractional blood volume.

The optimization-derived DBIF model [Wang et al., 2018] for analyzing dynamic liver PET data is shown in Fig. 2 and can be described using the following expressions:

$$u(t) = C_{\mathrm{A}}(t), \tag{10}$$

$$\boldsymbol{c}(t) = [C_{\mathrm{f}}(t), C_{\mathrm{m}}(t), C_{\mathrm{PV}}(t)]^T, \tag{11}$$

$$\boldsymbol{A} = \begin{bmatrix} -(k_2 + k_3) & k_4 & K_1(1 - f_A) \\ k_3 & -k_4 & 0 \\ 0 & 0 & -k_a \end{bmatrix}, \tag{12}$$

$$\boldsymbol{b} = [K_1 f_A, 0, k_a]^T, \tag{13}$$

$$\boldsymbol{w} = [1 - v_b, 1 - v_b, v_b(1 - f_A)]^T, \tag{14}$$

$$v \quad = v_b f_A \tag{15}$$

where $C_{\mathrm{A}}(t)$ denotes the blood input function extracted from the hepatic artery; $C_{\mathrm{PV}}(t)$ is the portal vein input function; k_a is the rate constant with which FDG flows through the gastrointestinal system. f_A is the fraction of hepatic artery contribution to the overall liver blood flow. The parameters to be determined are $\boldsymbol{\theta} = [v_b, K_1, k_2, k_3, k_4, k_a, f_A]^T$.

2.2. Laplace transform for structural identifiability analysis

The Laplace transform method is a popular method in the field of system theory for analyzing differential equations [Oppenheim et al., 1996, Tsien, 1954]. After the transform, the time derivative $\partial/\partial t$ becomes a multiplication of frequency s, thus simplifying the mathematical analysis. Taking the Laplace transform of equations (1) - (2) and making use of equation (3), one has

$$s\tilde{\boldsymbol{c}}(s) = \boldsymbol{A}\tilde{\boldsymbol{c}}(s) + \boldsymbol{b}\tilde{u}(s), \tag{16}$$

$$\tilde{o}(s) \quad = \boldsymbol{w}^T\tilde{\boldsymbol{c}}(s) + v\tilde{u}(s), \tag{17}$$

where

$$\tilde{f}(s) = \int_0^\infty f(t)e^{-st}\mathrm{d}t \tag{18}$$

represents the Laplace transform of any function f in the time domain.

The system input-output relation can then be expressed as

$$\tilde{o}(s) = \Phi(s)\tilde{u}(s), \tag{19}$$

where $\Phi(s)$ is called the transfer function in the frequency domain,

$$\Phi(s) = \left[\boldsymbol{w}^T(s\boldsymbol{I} - \mathbf{A})^{-1}\boldsymbol{b}\right] + v, \tag{20}$$

with $\boldsymbol{I}$ denoting the identity matrix. $\Phi(s)$ can be further expressed as a fractional function

$$\Phi(s) = \frac{N(s)}{D(s)}, \tag{21}$$

where both the numerator $N(s)$ and denominator $D(s)$ are a polynomial of the frequency s:

$$D(s) \triangleq \sum_{i=0}^{r} D_i s^i = \sum_{i=0}^{r} \alpha_i(\boldsymbol{\theta}) s^i, \tag{22}$$

$$N(s) \triangleq \sum_{i=0}^{r} N_i s^i = \sum_{i=0}^{r} \beta_i(\boldsymbol{\theta}) s^i, \tag{23}$$

with r being the highest order of the polynomials of s. N_i is the coefficient of order i in $N(s)$ and D_i is the coefficient of order i in $D(s)$. $\alpha_i(\boldsymbol{\theta})$ and $\beta_i(\boldsymbol{\theta})$ describe the theoretical model of N_i and D_i with respect to $\boldsymbol{\theta}$, respectively.

The structural identifiability analysis examines if the unknown parameter set $\boldsymbol{\theta}$ can be uniquely determined from $\{N_i, D_i\}_{i=0}^r$ following the equation set:

$$\alpha_i(\boldsymbol{\theta}) = D_i, \tag{24}$$

$$\beta_i(\boldsymbol{\theta}) = N_i, \tag{25}$$

for i from 0 to r. If there are arbitrary solutions for the equations, the model structure is non-identifiable. If the equations have a unique solution for any admissible input and in the whole parameter space, the model structure is called globally identifiable. If the solution only holds unique for a neighborhood of some points $\boldsymbol{\theta}_*$ in the parameter space, the structure is then locally identifiable.

2.3. Structural identifiability of single-input kinetic model

Substituting equations (4) - (9) into equation (20), we have

$$D(s) = s^2 + \alpha_1 \cdot s + \alpha_0, \tag{26}$$
$$N(s) = \beta_2 \cdot s^2 + \beta_1 \cdot s + \beta_0, \tag{27}$$

where the coefficients are defined by

$$\alpha_1 = k_2 + k_3 + k_4, \tag{28}$$
$$\alpha_0 = k_2 k_4, \tag{29}$$
$$\beta_2 = v_b, \tag{30}$$
$$\beta_1 = (1 - v_b)K_1 + v_b(k_2 + k_3 + k_4), \tag{31}$$
$$\beta_0 = (1 - v_b)K_1(k_3 + k_4) + v_b k_2 k_4. \tag{32}$$

Using the equation set $\alpha_i = D_i$ and $\beta_i = N_i$, we can obtain a unique solution for $\boldsymbol{\theta}$ after some algebraic operations:

$$v_b = N_2, \tag{33}$$
$$K_1 = \frac{N_1 - v_b D_1}{1 - v_b}, \tag{34}$$
$$k_2 = D_1 - \frac{(N_0 - v_b D_0)}{(1 - v_b)K_1}, \tag{35}$$
$$k_4 = \frac{D_0}{k_2}, \tag{36}$$
$$k_3 = D_1 - k_2 - k_4. \tag{37}$$

Therefore, the traditional SBIF three-compartmental model structure is globally identifiable in the parameter space.

2.4. Structural identifiability of dual-input kinetic modeling

For the optimization-derived DBIF model, the numerator and denominator of the transfer function $\Phi(s)$ are given by

$$D(s) = s^3 + (k_a + \alpha_1) \cdot s^2 + (k_a \alpha_1 + \alpha_0) \cdot s + k_a \alpha_0, \tag{38}$$
$$N(s) = \beta_2 f_A \cdot s^3 + (k_a \beta_2 + f_A \beta_1) \cdot s^2 + (k_a \beta_1 + f_A \beta_0) \cdot s + k_a \beta_0 \tag{39}$$

where $\{\alpha_i, \beta_i\}$ are defined by equations (28)-(32). The equation set to determine $\boldsymbol{\theta}$ is:

$$k_a + \alpha_1 = D_2, \tag{40}$$
$$k_a \alpha_1 + \alpha_0 = D_1, \tag{41}$$

$$k_a\alpha_0 = D_0, \tag{42}$$
$$\beta_2 f_A = N_3, \tag{43}$$
$$k_a\beta_2 + f_A\beta_1 = N_2, \tag{44}$$
$$k_a\beta_1 + f_A\beta_0 = N_1, \tag{45}$$
$$k_a\beta_0 = N_0, \tag{46}$$

Using equations (40) - (42), we can derive

$$k_a^3 - D_2k_a^2 + D_1k_a - D_0 = 0, \tag{47}$$

which is a cubic equation of k_a. In the real parameter space, the number of roots for k_a is at least 1 and at most 3. Similarly, we can derive f_A using equations (43) - (46),

$$N_0f_A^3 - (N_1k_a)\cdot f_A^2 + (N_2k_a^2)\cdot f_A - N_3k_a^3 = 0, \tag{48}$$

which is also a cubic equation when k_a is fixed. The number of roots for f_A in the non-negative parameter space is at least 1 and at most 3.

These results indicate that k_a and f_A are not globally identifiable because they may have multiple solutions. However, given there is at least one nonnegative root for k_a and f_A, they are locally identifiable. In practice, this requires a proper definition of initial estimates, lower and upper bounds for the parameters. Once k_a and f_A are determined, all α_i and β_i are determined. K_1, k_2, k_3, k_4 can then be determined from α_i and β_i as the same as in the single-input kinetic modeling.

3. Practical identifiability analysis using Monte Carlo simulation

3.1. Monte Carlo simulation

3.1.1. Overall description The process of the Monte Carlo simulation is described in figure 3. For each simulation, the nominal kinetic parameters $\boldsymbol{\theta}_0$ and the input function $C_A(t)$ were extracted from one of the human patient datasets and used to generate the noise-free liver tissue time activity curves (TAC). Independently and identically distributed noise was then added to the noise-free TAC following a defined noise model to generated $N = 1000$ realizations of noisy tissue TAC. We then fit the noisy liver tissue TACs and estimate the kinetic parameters using the optimization-derived DBIF kinetic model and the noisy aortic input function. Bias and standard deviation (SD) were calculated to assess the statistical properties of each kinetic parameter estimation. This Monte Carlo simulation was repeated for multiple patient data sets.

3.1.2. Human liver FDG kinetics and histological data Fourteen patients with NAFLD were included in this study to provide nominal kinetic parameters. These patients had a liver biopsy as a part of routine clinical care or for enrollment in clinical trials. Liver biopsies were scored according to the nonalcoholic steatohepatitis clinical research network (NASH-CRN) criteria. The scores of lobular inflammation and ballooning degeneration are combined to create an overall "liver inflammation" score (range 0-5). Dynamic PET studies were performed using

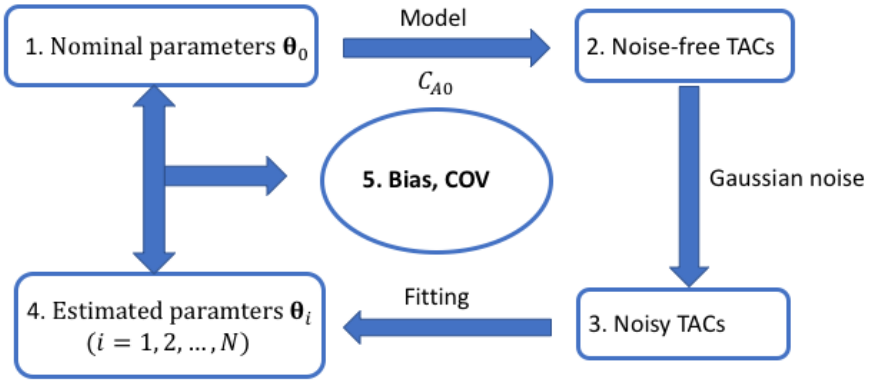

Figure 3. Flowchart of the practical identifiability analysis using Monte Carlo simulation.

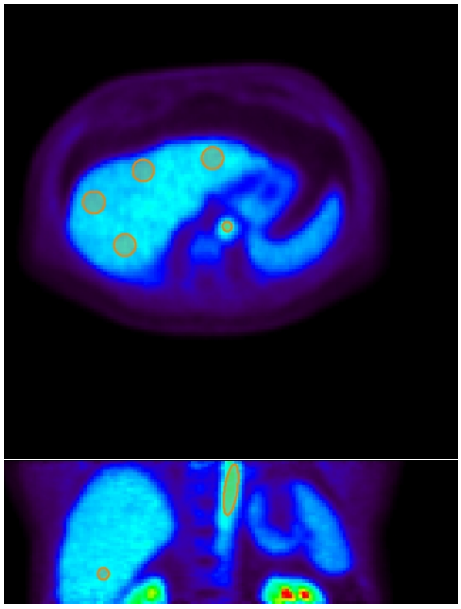

Figure 4. Illustration of volumetric ROIs in the liver segments and aorta in 2D planes. Top: a transverse plane showing the aortic ROI and four of eight spherical liver ROIs; Bottom: a coronal plane showing the aortic ROI and one of eight spherical liver ROIs. ROIs are overlayed on the PET image of one-hour duration. All the spherical liver ROIs are of 25 mm in diameter.

the GE Discovery 690 PET/CT scanner at the UC Davis Medical Center. Each patient was injected with 10 mCi ^{18}F-FDG and scanned for one hour, followed by a transmission CT scan for attenuation correction at the end of PET scan. Dynamic PET data were reconstructed into 49 time frames (30 x 10s, 10 x 60s, and 9 x 300s) using the vendor software with the standard ordered subsets expectation maximization algorithm with 2 iterations and 32 subsets.

Eight spherical regions of interest (ROI), each with 25 mm in diameter, were placed on eight segments of the liver excluding the caudate lobe and avoiding any major blood vessels. An illustration is shown in Figure 4. A TAC was extracted from each liver-segment ROI. The average of these TACs was used to represent the tissue TAC in the whole-liver region. An additional volumetric ROI was placed in the descending aorta region to extract image-derived

aortic input function. The optimization-derived DBIF model was used to derive the regional liver FDG kinetics at both the whole-liver ROI level and liver-segment ROI level. Hence there are a total 14 whole-liver FDG kinetic parameter sets and 112 liver-segment kinetic parameter sets from the 14 patient scans.

3.1.3. Noise model of TACs The reconstructed time activity in the frame m, c_m, can be approximately modeled by an i.i.d. Gaussian distribution [Wu and Carson, 2002, Carson et al., 1993],

$$c_m \sim \text{Gaussian}\Big(\bar{c}_m, S_c \cdot \delta_m\Big) \tag{49}$$

where $\{\bar{c}_m\}$ denotes the noise-free TAC and S_c is a scaling factor adjusting the amplitude of the unscaled standard deviation δ_m,

$$\delta_m = \sqrt{\frac{\bar{c}_m \exp(\lambda t_m)}{\Delta t_m}}, \tag{50}$$

where t_m is the mid-time of frame m, Δt_m is the scan duration of the time frame m, and $\lambda = \ln 2/T_{1/2}$ is the decay constant of radiotracer with $T_{1/2}$ (min) being the half-life. For ^{18}F-FDG, $T_{1/2} = 109.8$ minutes.

Equivalently, the normalized residual difference follows a zero-mean Gaussian with the standard deviation S_c:

$$\Delta c_m \triangleq \frac{c_m - \bar{c}_m}{\delta_m} \sim \text{Gaussian}(0, S_c). \tag{51}$$

From our patient study, we have a total 14 patients $\times$ 49 frames/patient $=$ 686 samples for Δc_m extracted at the whole-liver ROI level. The scale S_c can then be determined by approximating the histogram of Δc_m using the Gaussian with the standard deviation S_c. Similarly, we have a total 686$\times$ 8 = 5488 samples to estimate S_c for the noise level at the liver-segment ROI level.

3.2. Analysis methods

3.2.1. Sensitivity analysis The normalized sensitivity of a model TAC $C_{\text{T}}(t)$ with regard to a kinetic parameter θ_k is defined by

$$S_{\theta_k}(t) = \frac{\delta C_{\text{T}}(t)/C_{\text{T}}(t)}{\delta\theta_k/\theta_k} = \frac{\partial C_{\text{T}}(t)}{\partial \theta_k} \cdot \frac{\theta_k}{C_{\text{T}}(t)} \tag{52}$$

where k denotes the kth element of the kinetic parameter set $\boldsymbol{\theta}$ and $\partial C_{\text{T}}(t)/\partial\theta_k$ denotes the partial derivative of $C_{\text{T}}(t)$ with respect to θ_k. The normalized sensitivity function illustrates how much the model TAC would change in response to a small change $\delta\theta_k$ in the individual parameter θ_k. We evaluated the sensitivity functions for the mean of the kinetic parameters of the 14 patient datasets.

3.2.2. Quantification of bias and SD of kinetic parameters For each true kinetic parameter θ_k^0, the percent bias and SD of the kinetic parameter estimate $\hat{\theta}$ are calculated as

$$\text{Bias}(\hat{\theta}_k) = \frac{\text{Mean}(\hat{\theta}_k) - \theta_k^0}{\theta_k^0} \times 100\% \tag{53}$$

$$\text{SD}(\hat{\theta}_k) = \frac{1}{\theta_k^0}\sqrt{\frac{1}{N-1}\sum_{n=1}^{N}[\hat{\theta}_k - \text{Mean}(\hat{\theta}_k)]^2} \times 100\% \tag{54}$$

where Mean$(\cdot)$ represents the mean of the kinetic parameter estimates $\hat{\theta}_k$, respectively.

3.2.3. Comparison of different fitting options The initial values of the kinetic parameter set $[v_b, K_1, k_2, k_3, k_4, k_a, f_A]$ were set to [0.01, 1.0, 1.0, 0.01, 0.01, 1, 0.01] with lower bound [0, 0, 0, 0, 0, 0, 1, 0] and upper bound [1, 10, 10, 1, 0.1, 10, 1]. The weighting factor for the fitting was also initially set to be uniform as used in our previous study [Wang et al., 2018]. Nevertheless, our initial analysis indicates that this initialization may result in significant bias in K_1 for some patient datasets. To solve this problem, we proposed two modifications to improve the fitting and K_1 quantification. Instead of using a single initial value 1.0, we repeated the TAC fitting using different K_1 initial values (0.5, 1.0, 1.5, 2.0, 2.5, 3.0). The one with minimum least-squares of TAC fitting was used as the optimal. This modification can reduce the effect of getting stuck at a local solution of K_1. In addition, we also tested a nonuniform weighting scheme $w_m = \Delta t_m \cdot \exp(-\lambda \cdot t_m)$ versus the uniform weighting scheme $w_m = 1$. As K_1 is the major parameter of interest, these different approaches were compared for reducing the bias of K_1.

3.2.4. Parameter estimation accuracy over clinical range In addition to evaluating the bias and SD for each individual kinetic data set, we also evaluated the overall performance of the model over a wide parameter range following the approach used in [Mankoff et al., 1998]. We conducted a Pearson's linear correlation analysis to assess the closeness between θ_k^0 and $\hat{\theta}_k$ of all patients. The closer the correlation coefficient r is to 1, the more reliable the parameter can be estimated by the model over a wide range. In this study, we used the liver-segment kinetic parameter sets to allow a wide range of valuates to form the correlation plot.

3.2.5. Variation of the correlation between FDG K_1 and liver inflammation Our previous study of a patient cohort of 14 patients had demonstrated that the FDG K_1 parameter correlated with histological liver inflammation score with a statistical significance. Here we evaluate the reliability and uncertainty associated with the correlation between PET K_1 and histology. This is done by repeating the estimation of 14 patient kinetic parameter sets at the whole-liver ROI level for $N = 1000$ noisy realizations using the Monte Carlo simulation study (Fig. 3). The linear correlation r between liver inflammation score and K_1 is calculated for each realization. The bias, standard deviation and 95% confidence interval of r were then calculated to assess the reliability.

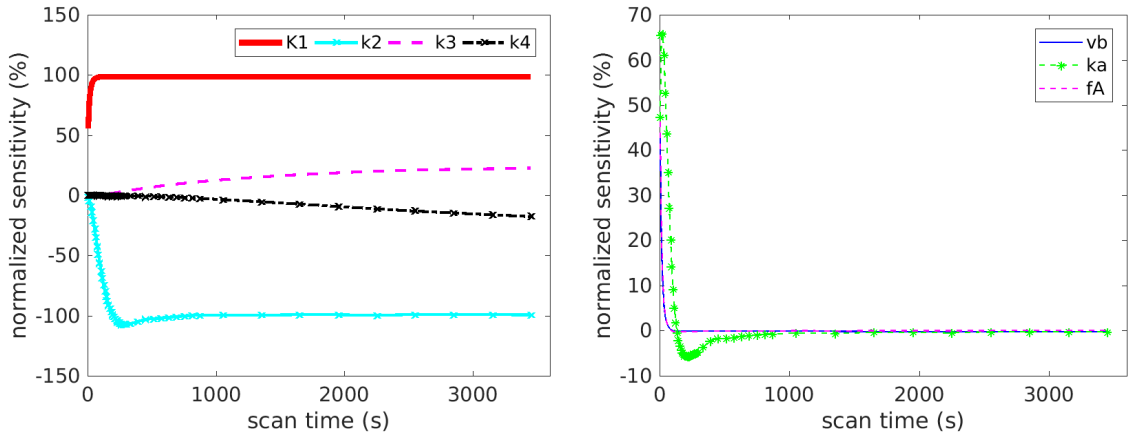

Figure 5. Normalized sensitivity functions representing percent change in model TAC $C_{\mathrm{T}}(t)$ in response to the change in kinetic parameters (a) K_1, k_2, k_3, k_4 and (b) v_b, k_a, f_A.

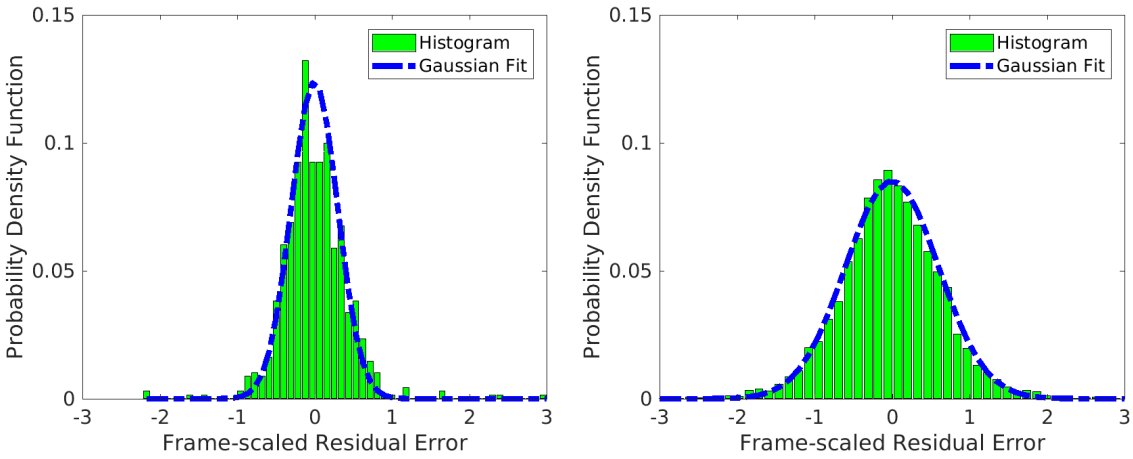

(a) whole-liver ROI level (b) liver-segment ROI level

Figure 6. Fit of the histogram of normalized residual difference Δc_m using a Gaussian distribution with the standard deviation S_c. (a) whole-liver ROI level, $S_c = 0.3$; (b) liver-segment ROI level, $S_c = 0.6$.

3.3. Results

3.3.1. Sensitivity analysis Figure 5 shows the plots of normalized sensitivity functions for different kinetic parameters in the optimization-derived DBIF model. The parameter set was the population means $\bar{\boldsymbol{\theta}} = [0.0185, 1.0013, 1.1400, 0.0149, 0.0586, 1.9849, 0.0405]^T$. The plots of v_b, k_a, f_A are zoomed in for the first ten minutes for better demonstration of the differences. The sensitivity curves of K_1, k_2 and other vascular-related kinetic parameters v_b, k_a, f_A become very stable after $t = 15$ minutes, indicating the early-time data dominate the estimation of these parameters. In comparison, the curves of k_3 and k_4 keep increasing or decreasing in the first 60 minutes, suggesting the estimation of these two parameters needs a sufficient long scan. K_1 and k_2 had opposite effect on the overall uptake with greater

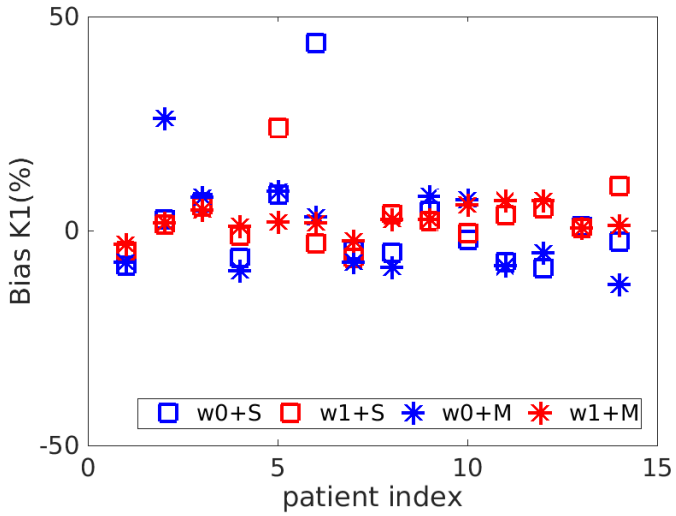

Figure 7. Bias in K_1 estimated using different fitting options. S refers to use single initial value for K_1 and M refers to use multiple initial values. w0 means the uniform weighting scheme and w1 means the nonuniform weighting scheme.

contributions than k_3 and k_4. The absolute sensitivity of K_1 is different from that of k_2 mainly in the early time.

The sensitivity curves of v_b, k_a, f_A become nearly zero after $t = 15$ minutes, suggesting the late time data contribute trivial to the estimation of these parameters. The curve of v_b is almost fully overlapped with that of f_A. This indicates it is difficult to differentiate them from each other. Because the curve shape of v_b or f_A is different from the shape of K_1, the coupled effect of v_b and f_A should have a minimal effect on the estimation of K_1.

3.3.2. Determination of the noise model parameter Figure 6 shows the histograms of the normalized residual error Δc_m at the whole-liver ROI level and the liver-segment ROI level. The obtained S_c values are 0.3 and 0.6, respectively. The distribution of Δc_m approximately follows a Gaussian well in both cases. We therefore used these two S_c values to define the noise standard deviation for the whole-liver ROI level and liver-segment level in the simulation studies. Note that the size of whole-liver ROI is 8 times that of the liver-segment ROI, which is supposed to reduce the noise standard deviation by a factor of $\sqrt{8} \approx 2.8$. However, pixels in the liver ROI are not fully independent of each other and therefore the reduction in S_c can be smaller than that by the ROI size increase.

3.3.3. Comparison of different fitting options Figure 7 shows the comparison of different initialization and weighting schemes for each patient at the whole-liver ROI level ($S_c = 0.3$). The K_1 single-initialization strategy resulted in bias in K_1 in several patient datasets. The bias can be reduced when the multi-initialization strategy was used, which however did not provide a universal improvement over all patients. On the other hand, use of nonuniform weighting for TAC fitting led to reduced bias in some patients. The benefit of these two modifications were

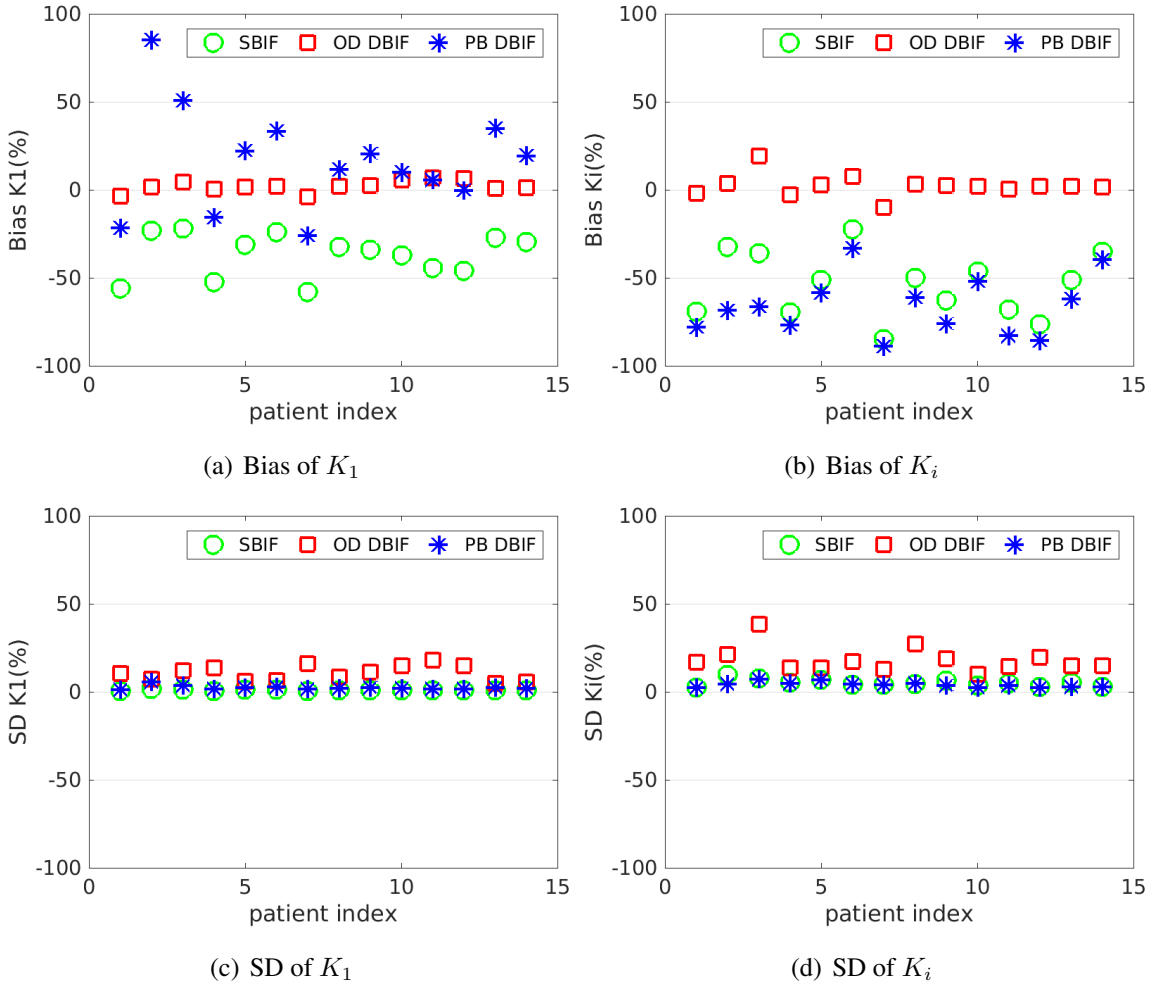

(a) Bias of K_1 (b) Bias of K_i

(c) SD of K_1 (d) SD of K_i

Figure 8. Bias and SD of K_1 and K_i estimates in the optimization-derived (OD) DBIF model for 14 patient data sets with $S_c = 0.3$, as compared with the inaccurate SBIF model and population-based (PB) DBIF model.

maximized when they were used together and the bias in K_1 remained small in all patients. Thus, the multi-initialization for K_1 and nonuniform weighting scheme were used in this work for all subsequent analysis.

3.3.4. Bias of inappropriate kinetic models Figure 8 show the bias and SD of K_1 and K_i estimated by three different kinetic models at the noise level of $S_c = 0.3$. When the traditional SBIF model was used for fitting the TAC which essentially follows the DBIF model, K_1 was underestimated with an average 37% bias. K_1 by the population-based DBIF was also underestimated by 26%. In comparison, the mean absolute bias of K_1 by the optimization-derived DBIF model was only about 3% and the biases of individual patients all remain small. For the estimation of K_i, the SBIF and population-based DBIF resulted in an underestimation of approximately 60%, as compared with an average bias of less than 5% by the optimization-derived DBIF model.

The bias reduction achieved by the optimization-derived DBIF model came with the

	OD DBIF		SBIF		PB DBIF	
	Bias (%)	SD(%)	Bias(%)	SD(%)	Bias(%)	SD(%)
K_1	3.2	10.8	36.7	1.1	25.5	2.6
k_2	3.5	11.6	40.1	1.1	21.7	2.4
k_3	5.0	19.7	56.1	5.2	69.4	4.0
k_4	8.1	44.0	85.1	9.4	90.7	8.5
K_i	4.5	18.3	53.8	5.2	66.1	4.2

Table 1. Absolute bias and SD of liver FDG kinetic parameter estimates by different kinetic models. The absolute bias and SD are averaged over 14 patient data sets.

	$S_c = 0$		$S_c = 0.3$		$S_c = 0.6$	
	Bias (%)	SD(%)	Bias(%)	SD(%)	Bias(%)	SD(%)
K_1	0.6	0	3.2	10.8	7.4	18.3
k_2	0.6	0	3.5	11.6	8.2	19.6
k_3	0.2	0	5.0	19.7	12.4	40.3
k_4	0.1	0	8.1	44.0	22.7	81.6
K_i	0.2	0	4.5	18.3	11.1	37.0
v_b	16.2	0	71.8	206.5	182.6	484.6
k_a	0.6	0	3.9	16.2	6.1	27.6
f_A	16.9	0	38.3	121.9	41.6	142.5

Table 2. Bias and SD of the kinetic parameters in the optimization-derived DBIF model under three different noise levels: $S_c = 0$ (noise-free), $S_c = 0.3$ (whole-liver ROI level), and $S_c = 0.6$ (liver-segment ROI level).

price of increased SD, as shown in Figure 8(c) and (d). The average SD was 11% for K_1 and 18% for K_i by the optimization-derived DBIF, as compared to less than 6% by the other two models. This can be explained by the increased number of free parameters in the optimization-derived DBIF model.

The results of the averaged absolute bias and SD across different patients are summarized in table 1 for all FDG transport rate parameters. Generally, with the assumption of the TACs following the DBIF model, the inaccurate SBIF model resulted in greater than 35-85% bias and the population-based DBIF model led to greater than 20-90% bias in all kinetic estimates. The accurate optimization-derived DBIF model still had a bias of about 3-8% in all the kinetic estimates, which can be explained by the facts that noise propagation is highly nonlinear and the structural identifiability of the model is local.

Note that as compared to the SBIF and population-based DBIF models, the increase of SD by the optimization-derived DBIF model was generally smaller than the corresponding bias reduction. This indicates the overall gain of the new model is greater than its loss, which led to the improvement in correlating FDG K_1 with histology as we observed in the previous patient study [Wang et al., 2018].

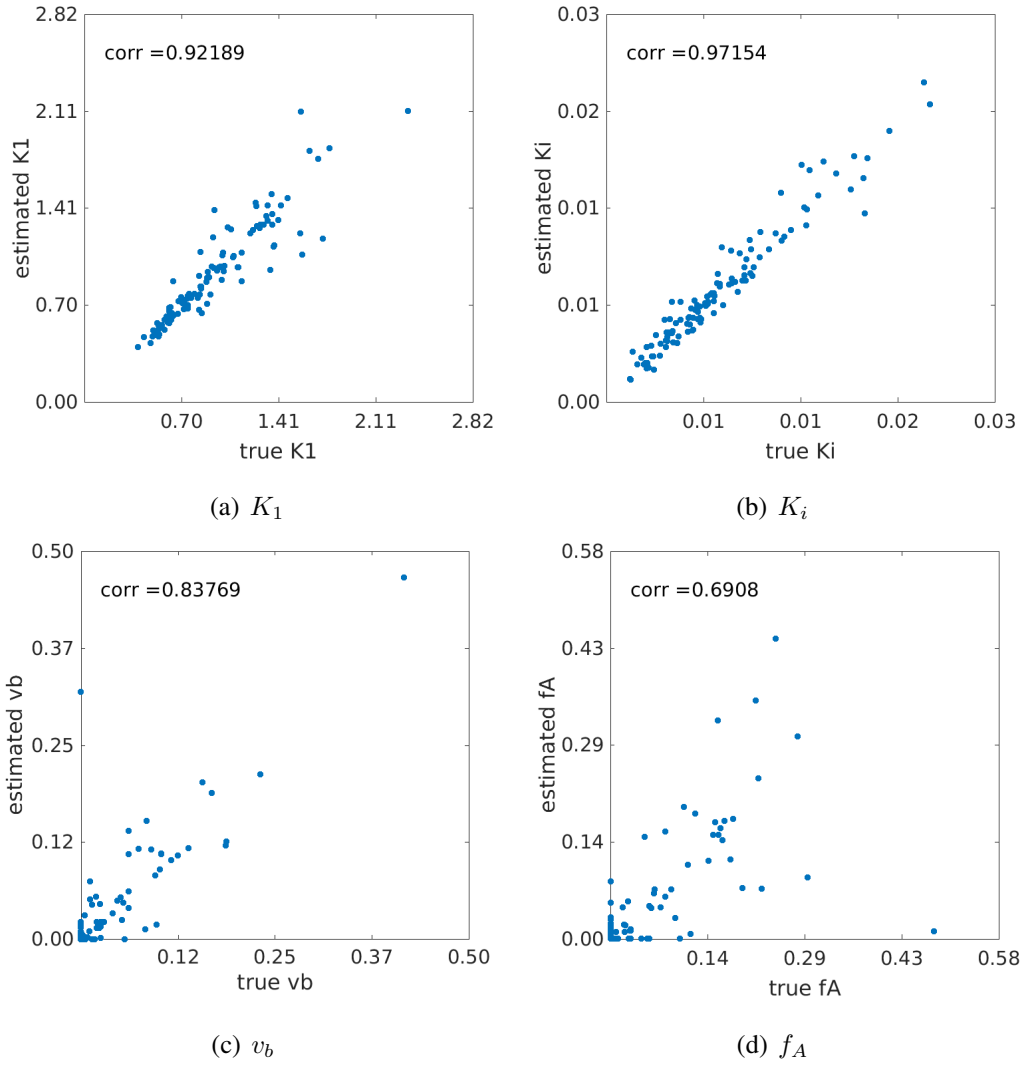

(a) K_1 (b) K_i

(c) v_b (d) f_A

Figure 9. Correlation between the true kinetic parameter values and estimated values from noisy data ($S_c = 0.3$). (a) K_1, (b) K_i, (c) v_b and f_A.

3.3.5. Effect of noise levels on kinetic quantification Table 2 shows the average absolute bias and SD of kinetic parameters estimated by the optimization-derived DBIF model under three noise levels: noise-free ($S_c = 0.0$), noise at the whole-liver ROI level ($S_c = 0.3$), and noise at the liver-segment ROI level ($S_c = 0.6$). While other kinetic parameters had a small bias, the bias of v_b and f_A were surprisingly large even at the noise-free case ($S_c = 0.0$). This can be explained by the fact that the model is locally identifiable with potential multiple solutions. The result is also consistent with the observation on the indifferentiable sensitivity curves of v_b and f_A in figure 5. Despite the large bias in v_b and f_A, the bias of K_1 remained small (<8%). The SD of K_1 increased from 7% to 18% when the noise level was changed from the whole-liver ROI level to liver-segment ROI level. The estimation of K_i is more sensitive to noise, with the SD being 18% for the whole-liver ROI level and 37% for the liver-segment ROI level. k_2 had similar accuracy and precision as K_1 and k_3 had similar accuracy and precision as K_i. k_4 had a much higher bias and SD because the scan time (1-hour in our study) is not

	v_b	K_1	k_2	k_3	k_4	k_a	f_A	K_i
$S_c = 0.3$	0.84	0.92	0.90	0.97	0.98	0.91	0.69	0.97
$S_c = 0.6$	0.78	0.88	0.83	0.90	0.91	0.79	0.66	0.90

Table 3. Coefficients of the linear correlation between estimated kinetic parameters and their true values.

sufficient enough for robust estimation of k_4, which can justified from its sensitivity curve.

3.3.6. Parameter estimation accuracy over clinical range Figure 9 shows the plots of linear correlation between the true values and noisy estimates of different kinetic parameters at the whole-liver ROI noise level. The correlation coefficients under different noise levels for all kinetic parameters are summarized in table 3. As the noise level increased, the correlation coefficients reduced. Both K_1 and K_i were well repeatable against noise. While all other kinetic parameters including (k_2, k_3, k_4, k_a) can be repeated well, the two vascular parameters v_b and f_A are less repeatable.

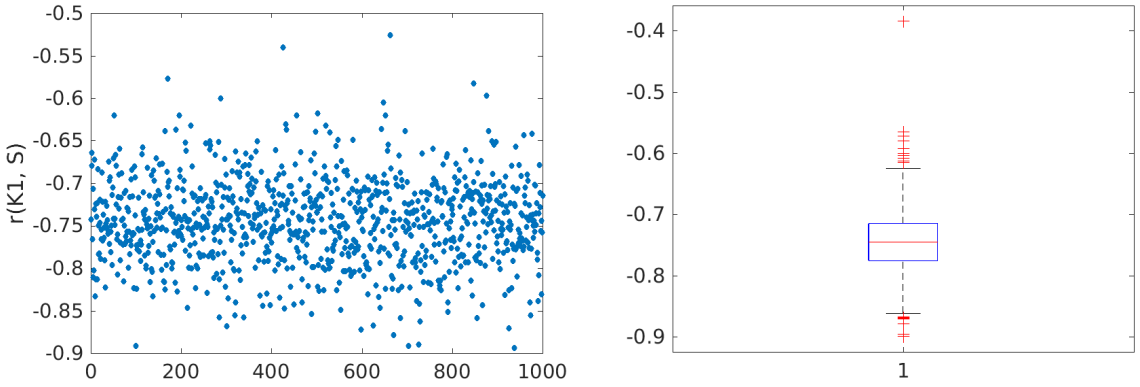

(a) (b)

Figure 10. Noise variation of the correlation r between FDG K_1 and histological liver inflammation score. (a) r values of 1000 noisy realizations, (b) box plot of the r values.

3.3.7. Noise variation of the K_1 correlation with liver inflammation Figure 10 shows the results of correlating the histological inflammation scores with the FDG K_1 estimates derived from 1000 noisy realizations ($S_c = 0.3$). The linear correlation r between the original K_1 values and liver inflammation scores in the cohort of 14 patients was r =-0.7618 (p=0.0012). The 95% confidence interval of the noisy r estimates was estimated to be [-0.8434, -0.6494] with the mean -0.7452 and standard derivation 0.0493. The percent bias in r was -2.2% and the SD was 6.5%, both approximately close to that in K_1. These results indicate the stability of the estimation of the correlation between FDG K_1 and liver inflammation.

	free k_a		fixed k_a	
	Bias (%)	SD(%)	Bias(%)	SD(%)
K_1	3.2	10.8	0.3	3.0
k_2	3.5	11.6	0.4	3.4
k_3	5.0	19.7	1.9	17.7
k_4	8.1	44.0	4.6	41.6
K_i	4.5	18.3	1.7	16.6
v_b	71.8	206.5	47.9	116.9
k_a	3.9	16.2	/	/
f_A	38.3	121.9	40.0	106.0

Table 4. Bias and SD of a typical kinetic parameter set (population means) estimated by the optimization-derived DBIF model with k_a freely estimated or fixed at its true value.

4. Discussion

FDG K_1 by the optimization-derived DBIF model is a promising PET biomarker for evaluating human liver inflammation in fatty liver disease [Wang et al., 2017, Sarkar et al., 2017, Wang et al., 2018]. The focus of this work is to characterize the identifiability of the optimization-derived DBIF model structure and evaluate the accuracy and precision of K_1 and other kinetic parameters in dynamic liver PET.

We first conducted a theoretical analysis of the structural identifiability of standard 3-compartmental model and the new DBIF model using the Laplacian transform. While standard 3-comaprtmental model is globally identifiable, the new model is locally identifiable due to potential multiple solutions. This suggests that it is worth being careful with defining the initial values, lower and upper bounds of kinetic parameter estimation to properly constrain the optimization problem of TAC fitting with the new model.

We then conducted Monte Carlo simulations to examine the practical identifiability of the model parameters based on 14 patient datasets which include both dynamic FDG-PET data and histopathology data of human liver inflammation. While the estimation of some kinetic parameters (e.g. f_A and v_b) is associated with large bias and standard deviation, FDG K_1, the parameter of major interest, has low bias ($\approx$3%) and standard deviation ($\approx$11%) at the whole-liver ROI level. As demonstrated in the simulation study, fitting liver TACs using the traditional SBIF model or the population-based DBIF model may result in significant bias (>20%) in liver K_1 quantification. These results explain why the K_1 by the new model achieved a statistically significant association with liver inflammation in the patient study, while the other two models did not demonstrate success [Wang et al., 2018].

We also examined the reliability of the new model for liver K_1 quantification over a wide range of values from 0.5 to 2.5 (Fig. 9). The true K_1 values and their estimates are highly correlated ($r > 0.9$). The stability of K_1 estimation against noise is also preserved in its correlation with liver inflammation (Fig. 10).

A disadvantage of the optimization-derived DBIF model is the increased standard

deviation in kinetic parameter estimation, which is basically caused by the increased number of free parameters. To control the standard deviation of K_1 and other parameters of interest, one potential strategy is to add additional constraints in the optimization problem. For example, Table 4 compares the bias and standard deviation of kinetic parameters for either estimating or fixing the input function parameter k_a in the optimization of TAC fitting. If k_a is fixed at its true values, the bias and standard deviation of K_1 (and other kinetic parameters) can be largely reduced. This is not surprising because a fixed k_a corresponds to a known portal vein input function. However, the result reported here indicates the potential improvement space if a modified method can be developed to incorporate the prior information of the portal vein input function.

The study also indicates that kinetic quantification at the liver-segment ROI noise level ($S_c = 0.6$) is less reliable than at the whole-liver ROI noise level ($S_c = 0.3$). Both bias and SD become nearly doubled, as shown in Table 2. It is worth noting that all the studies were conducted using standard clinical PET. Recently, high-sensitivity total-body PET scanner EXPLORER has been developed [Cherry et al., 2018]. The new generation scanner can increase sensitivity of PET by a factor of 4-5 for imaging a single organ [Poon et al., 2012]. The scanner sensitivity improvement will be able to reduce the liver-segment ROI noise level from current $S_c = 0.6$ to $S_c = 0.3$. Thus, quantification of liver segmental heterogeneity may become reliable on EXPLORER. Equivalently, the whole-liver ROI noise level may also be reduced from current $S_c = 0.3$ to $S_c = 0.15$ if EXPLORER is used. The resulting bias and SD of K_1 were 1.4% and 6.5%, respectively, according to our simulation study.

5. Conclusion

This paper has conducted both theoretical analysis of structural identifiability and Monte Carlo study of practical identifiability for the optimization-derived DBIF model in dynamic PET of liver inflammation. The theoretical analysis suggests that the parameters of the new model are identifiable but subject to local solutions. The simulation results have shown that the estimation of vascular kinetic parameters (v_b and f_A) suffer from high variation. However, FDG K_1 can be reliably estimated in the new optimization-derived DBIF model. The bias of K_1 by the new model is approximately 3% and the standard deviation is about 11% at the whole-liver ROI noise level. The estimated values and original values of K_1 are also highly correlated with each ($r = 0.92$). The correlation between liver K_1 by the new model and histological inflammation score is robust to noise interference. These results suggest that liver FDG K_1 quantification is reliable for clinical use to assess liver inflammation at the whole-liver ROI level. Future work will include further development of the DBIF modeling approach and use of EXPLORER for reduced bias and variance in K_1.

Reference

[Anderson, 1983] Anderson, D. (1983). *Compartmental Modeling and Tracer Kinetics*. Lecture Notes in Biomathematics. Springer Berlin Heidelberg.

[Audoly et al., 2001] Audoly, S., Bellu, G., D'Angio, L., Saccomani, M. P., and Cobelli, C. (2001). Global identifiability of nonlinear models of biological systems. *IEEE Trans Biomed Eng*, 48(1):55–65.

[Bellman and Astrom, 1970] Bellman, R. and Astrom, K. J. (1970). On structural identifiability. *Mathematical Biosciences*, 7:329–339.

[Brix et al., 2001] Brix, G., Ziegler, S. I., Bellemann, M. E., Doll, J., Schosser, R., Lucht, R., Krieter, H., Nosske, D., and Haberkorn, U. (2001). Quantification of [F-18]FDG uptake in the normal liver using dynamic PET: Impact and modeling of the dual hepatic blood supply. *Journal of Nuclear Medicine*, 42(8):1265–1273.

[Carson et al., 1993] Carson, R. E., Yan, Y., Daubewitherspoon, M. E., Freedman, N., Bacharach, S. L., and Herscovitch, P. (1993). An approximation formula for the variance of PET region-of-interest values. *IEEE Transactions on Medical Imaging*, 12(2):240–250.

[Cherry et al., 2018] Cherry, S. R., Jones, T., Karp, J. S., Qi, J. Y., Moses, W. W., and Badawi, R. D. (2018). Total-body PET: Maximizing sensitivity to create new opportunities for clinical research and patient care. *Journal of Nuclear Medicine*, 59(1):3–12.

[Doot et al., 2010] Doot, R. K., Muzi, M., Peterson, L. M., Schubert, E. K., Gralow, J. R., Specht, J. M., and Mankoff, D. A. (2010). Kinetic analysis of 18f-fluoride PET images of breast cancer bone metastases. *J Nucl Med*, 51(4):521–7.

[El Fakhri et al., 2009] El Fakhri, G., Kardan, A., Sitek, A., Dorbala, S., Abi-Hatem, N., Lahoud, Y., Fischman, A., Coughlan, M., Yasuda, T., and Di Carli, M. F. (2009). Reproducibility and accuracy of quantitative myocardial blood flow assessment with 82Rb PET: comparison with 13N-ammonia PET. *Journal of Nuclear Medicine*, 50(7):1062–1071.

[Gunn, 1996] Gunn, R. (1996). *Mathematical modelling and identifiability applied to positron emission tomography data*. PhD thesis, University of Warwick.

[Kalman, 1963] Kalman, R. E. (1963). Mathematical description of linear dynamical systems. *Journal of the Society for Industrial and Applied Mathematics Series A Control*, 1(2):152–192.

[Komorowski et al., 2011] Komorowski, M., Costa, M. J., Rand, D. A., and Stumpf, M. P. (2011). Sensitivity, robustness, and identifiability in stochastic chemical kinetics models. *Proc Natl Acad Sci U S A*, 108(21):8645–50.

[Kudomi et al., 2009] Kudomi, N., Jarvisalo, M. J., Kiss, J., Borra, R., Viljanen, A., Viljanen, T., Savunen, T., Knuuti, J., Iida, H., Nuutila, P., and Iozzo, P. (2009). Non-invasive estimation of hepatic glucose uptake from [18F]FDG PET images using tissue-derived input functions. *Eur J Nucl Med Mol Imaging*, 36(12):2014–26.

[Ljung and Glad, 1994] Ljung, L. and Glad, T. (1994). On global identifiability for arbitrary model parametrizations. *Automatica*, 30(2):265 – 276.

[Mankoff et al., 2006] Mankoff, D., Muzi, M., and Zaidiy, H. (2006). Quantitative analysis in nuclear oncologic imaging. In *Quantitative Analysis in Nuclear Medicine Imaging*, pages 494–536. Springer.

[Mankoff et al., 1998] Mankoff, D. A., Shields, A. F., Graham, M. M., Link, J. M., Eary, J. F., and Krohn, K. A. (1998). Kinetic analysis of 2-[carbon-11]thymidine PET imaging studies: compartmental model and mathematical analysis. *J Nucl Med*, 39(6):1043–55.

[Miao et al., 2008] Miao, H., Dykes, C., Demeter, L. M., Cavenaugh, J., Park, S. Y., Perelson, A. S., and Wu, H. (2008). Modeling and estimation of kinetic parameters and replicative fitness of HIV-1 from flow-cytometry-based growth competition experiments. *Bulletin of Mathematical Biology*, 70(6):1749–1771.

[Miao et al., 2011] Miao, H., Xia, X., Perelson, A. S., and Wu, H. (2011). On identifiability of nonlinear ode models and applications in viral dynamics. *SIAM Rev Soc Ind Appl Math*, 53(1):3–39.

[Michelotti et al., 2013] Michelotti, G. A., Machado, M. V., and Diehl, A. M. (2013). NAFLD, NASH and liver cancer. *Nat Rev Gastroenterol Hepatol*, 10(11):656–65.

[Munk et al., 2001] Munk, O. L., Bass, L., Roelsgaard, K., Bender, D., Hansen, S. B., and Keiding, S. (2001). Liver kinetics of glucose analogs measured in pigs by PET: Importance of dual-input blood sampling. *Journal of Nuclear Medicine*, 42(5):795–801.

[Musso et al., 2011] Musso, G., Gambino, R., Cassader, M., and Pagano, G. (2011). Meta-analysis: natural history of non-alcoholic fatty liver disease (NAFLD) and diagnostic accuracy of non-invasive tests for liver

disease severity. *Ann Med*, 43(8):617–49.

[Muzi et al., 2005] Muzi, M., Mankoff, D. A., Grierson, J. R., Wells, J. M., Vesselle, H., and Krohn, K. A. (2005). Kinetic modeling of 3'-deoxy-3'-fluorothymidine in somatic tumors: mathematical studies. *J Nucl Med*, 46(2):371–80.

[Muzi et al., 2006] Muzi, M., Spence, A. M., O'Sullivan, F., Mankoff, D. A., Wells, J. M., Grierson, J. R., Link, J. M., and Krohn, K. A. (2006). Kinetic analysis of 3'-deoxy-3'-18f-fluorothymidine in patients with gliomas. *J Nucl Med*, 47(10):1612–21.

[Oppenheim et al., 1996] Oppenheim, A. V., Willsky, A. S., and Nawab, S. H. (1996). *Signals &Amp; Systems (2Nd Ed.)*. Prentice-Hall, Inc., Upper Saddle River, NJ, USA.

[Pohjanpalo, 1978] Pohjanpalo, H. (1978). System identifiability based on the power series expansion of the solution. *Mathematical Biosciences*, 41(1):21 – 33.

[Poon et al., 2012] Poon JK, Dahlbom ML, Moses WW, et al. (2012). Optimal whole-body PET scanner configurations for different volumes of LSO scintillator: a simulation study solution. *Phys Med Biol*, 57:4077 – 4094.

[Raue et al., 2014] Raue, A., Karlsson, J., Saccomani, M. P., Jirstrand, M., and Timmer, J. (2014). Comparison of approaches for parameter identifiability analysis of biological systems. *Bioinformatics*, 30(10):1440–8.

[Rodriguez-Fernandez et al., 2006a] Rodriguez-Fernandez, M., Egea, J. A., and Banga, J. R. (2006a). Novel metaheuristic for parameter estimation in nonlinear dynamic biological systems. *BMC Bioinformatics*, 7(1):483.

[Rodriguez-Fernandez et al., 2006b] Rodriguez-Fernandez, M., Mendes, P., and Banga, J. R. (2006b). A hybrid approach for efficient and robust parameter estimation in biochemical pathways. *Biosystems*, 83(2):248 – 265. 5th International Conference on Systems Biology.

[Rothenberg, 1971] Rothenberg, T. J. (1971). Identification in parametric models. *Econometrica*, 39(3):577–591.

[Sarkar et al., 2017] Sarkar, S., Corwin, M., Olson, K., Stewart, S., Johnson, C. R., Badawi, R., and Wang, G. B. (2017). 4D dynamic FDG-PET correlates with hepatic inflammation and steatosis in patients with non-alcoholic steatohepatitis. *Hepatology*, 66:107a–108a.

[Sarkar et al., 2018] Sarkar, S., Corwin, M., Olson, K., Stewart, S., Liu, C., Badawi, R., and Wang, G. (2018). Pilot study to diagnose non-alcoholic steatohepatitis with dynamic 18F-fluorodeoxyglucose positron emission tomography. *American Journal of Roentgenology*, in press.

[Tsien, 1954] Tsien, H. (1954). *Engineering Cybernetics*. McGraw-Hill book Company, Incorporated.

[Walter and Lecourtier, 1981] Walter, E. and Lecourtier, Y. (1981). Unidentifiable compartmental models: what to do? *Mathematical Biosciences*, 56(1):1 – 25.

[Wang et al., 2017] Wang, G., Corwin, M., Olson, K., Stewart, S., Zha, C., Badawi, R., and Sarkar, S. (2017). Dynamic FDG-PET study of liver inflammation in non-alcoholic fatty liver disease. *Journal of Hepatology*, 66(1):S592.

[Wang et al., 2018] Wang, G., Corwin, M. T., Olson, K. A., Badawi, R. D., and Sarkar, S. (2018). Dynamic PET of human liver inflammation: impact of kinetic modeling with optimization-derived dual-blood input function. *Physics in Medicine and Biology*, 63(15):155004.

[Wree et al., 2013] Wree, A., Broderick, L., Canbay, A., Hoffman, H. M., and Feldstein, A. E. (2013). From NAFLD to NASH to cirrhosis-new insights into disease mechanisms. *Nat Rev Gastroenterol Hepatol*, 10(11):627–36.

[Wu and Carson, 2002] Wu, Y. J. and Carson, R. E. (2002). Noise reduction in the simplified reference tissue model for neuroreceptor functional imaging. *Journal of Cerebral Blood Flow and Metabolism*, 22(12):1440–1452.

[Xia and Moog, 2003] Xia, X. and Moog, C. H. (2003). Identifiability of nonlinear systems with application to HIV/AIDS models. *IEEE Transactions on Automatic Control*, 48(2):330–336.